Effective Models of Heat Conduction in Composite Electrodes

Journal of The Electrochemical Society, 2023 **170** 100503
1945-7111/2023/170(10)/100503/9/$40.00 © 2023 The Electrochemical Society ("ECS"). Published on behalf of ECS by IOP Publishing Limited

Effective Models of Heat Conduction in Composite Electrodes

Weiyu Li and Daniel M. Tartakovsky[z]

Department of Energy Science and Engineering, Stanford University, Stanford, California 94305, United States of America

Thermal effects impact battery performance, safety, and health. Existing models of heat generation, conduction, and dissipation in batteries account for distinct physicochemical properties of the active material and electrolyte but routinely disregard the presence of the carbon binder domain (CBD), which ensures the electrodes' cohesiveness and structural stability. We present a homogenized thermal model for a spherical active particle coated with CBD and immersed in a liquid electrolyte. The model replaces this composite particle with a homogeneous particle whose equivalent thermal conductivity and other properties preserve the amount of released heat and heat flux at the solid/electrolyte interface, for a given ambient temperature. The effective thermal conductivity is expressed in terms of the volume fraction of the active material in the mixture and the electrochemical and thermal properties of both the active material and CBD. This analytical expression for thermal conductivity can be readily integrated into thermal simulations at either device-scale or pore-scale, without adding computational complexity. Consequently, it provides a means to account for CBD in models used for battery design and management.
 [DOI: 10.1149/1945-7111/acfdd4]

Manuscript submitted August 17, 2023; revised manuscript received September 13, 2023. Published October 9, 2023.

Thermal effects play a crucial role in the performance, safety, and overall health of batteries. Heat is generated during both charging and discharging, which increases a battery's internal temperature. Major heat sources include the irreversible Joule/Ohmic heating in the electrode and electrolyte, irreversible reaction heat, and reversible entropic heat at the electrode/electroyte interfaces.[1,2] The accumulation of excessive heat within the battery can have adverse effects such as electrolyte decomposition and thermal runaway.[3,4] Quantitative understanding of heat conduction, generation and dissipation is necessary to uncover the impact of electrodes' microstructure on a battery's thermal behavior at the microscale,[5] to characterize thermal properties at the cell level, and to implement efficient thermal management at the system level.[6,7] Additionally, electrochemical reactions and transport properties (diffusion coefficient, conductivity) are temperature sensitive.

The vast majority of experimental research on thermal phenomena in batteries is conducted at the cell and system levels, including cell-level thermal abuse measurements and thermal runaway propagation in battery packs.[8–12] The relative paucity of experimental studies at the micro-scale[13,14] is primarily due to technical challenges of mapping out the internal temperature field through non-destructive in situ measurements.[15] In this situation, mathematical modeling presents a viable tool to estimate the internal temperature distribution within a cell. Despite their importance, most of such models are relatively low-fidelity. Representative examples include lumped-parameter models[5,16–18] or models that treat the cell's components as homogenized.[19–21] While these models often yield accurate assessment of the overall cell and system performance, they are not designed to capture the intricate effects of a battery's microstructure. They fail to adequately represent thermal processes at the particle level and heat generation at the electrolyte-solid interfaces, e.g., the formation of local hotspots. Further refinements of modeling approaches are needed to account for these microstructural complexities and to improve the understanding of battery thermal behavior. Several studies have emphasized the significance of improving the prediction of effective thermal conductivity of battery components.[22–24]

The ubiquitous presence of binder and conducting carbon, collectively known as the carbon binder domain (CBD), introduces additional complications. CBD is used in lithium-ion and lithium-metal batteries to improve the mechanical integrity and electrical conductivity of their electrodes. Previous studies have illustrated CBD's effects on mass and charge transport in the electrodes,[25,26] but its influence on thermal conduction remains unexplored, even though it has the potential to act as either a heat insulator or a heat conductor within the electrode structure. Therefore, it is necessary to develop a mathematical model that relates measurable characteristics of active particles and CBD, such as their volume fractions and thermal properties (thermal conductivities, heat capacities, etc.) to the bulk thermal properties (thermal conductivities, heat capacities, etc.) of the composite electrode material. Existing theoretical relations, such as Wiener bounds or Hashin-Shtrikman bounds,[27] are inadequate to determine the effective thermal conductivity of the battery electrodes because they do not guarantee the energy conservation in the presence of various heat generation sources that are coupled with mass and charge transport in the electrode.

We address the aforementioned challenges by presenting an equivalent/homogenized model of heat transfer in a spherical active particle coated by CBD and immersed in a liquid electrolyte. The model accounts for multiple sources of heat generation, including the Joule-Ohmic heating and entropic heating, which occur within the electrode and CBD and at their interfaces. The model ensures the global conservation of mass, energy, and charge. A key outcome of our model is a semi-analytical expression for the effective thermal conductivity of the homogeneous particle, which comprises the volume fractions and transport properties of the constitutive phases and takes a closed form at large time. This result, coupled with the derivation of the effective ionic diffusivity and electrical conductivity,[25] completes a comprehensive study of effective physicochemical properties of composite (active-material/CBD) electrodes.

Our effective heat transfer model can be integrated into existing thermal models at the device level to investigate the impact of the CBD's physical properties (thermal conductivity, volume fraction, etc.) on heat transfer within the battery cell. Our model can also be deployed in pore-scale simulations by lumping together the active material and CBD. Our analytical expression offers a distinct advantage, as it can be directly used in these models without adding computational complexity. Our research contributes to the advancements in battery technology by providing a deeper understanding of the thermal aspects of composite electrodes. By considering the complex interplay between heat transfer, ion diffusion and intercalation, and charge transport, our electrochemical-thermal model provides a valuable tool for optimization of the fractions of each component in the composite electrode to enhance the overall battery performance.

Problem Formulation

Our effective heat-transfer model is formulated in a manner consistent with the previous study of mass and charge transport in composite electrodes.[25] We consider a spherical active particle of radius r_1 that is coated with a CBD layer, giving rise to a composite sphere of radius r_2 (Fig. 1). The active material has diffusion coefficient D_1 (m^2/s), ionic conductivity K_1 (S/m), density ρ_1

[z]E-mail: tartakovsky@stanford.edu

(kg/m^3), heat capacity c_{p_1} (J/kg/K), and thermal conductivity λ_1 (W/m/K); the corresponding quantities for CBD are denoted by D_2, K_2, ρ_2, c_{p_2} and λ_2. Li-ion intercalation takes place at the active particle's surface, i.e., at $r = r_1$, which induces reaction heat flux $\mathcal{Q}_{reac}$ (J/m^2/s) and entropic heat flux $\mathcal{Q}_{entr}$ (J/m^2/s).[1] The sphere is immersed in an electrolyte with Li-ion concentration c_e (mol/m^3), electric potential ϕ_e (V) and temperature T_e (K); uniform electric field $\mathbf{E}$ in the x direction represents electric field in a working battery's electrode. Ionic resistance under the electric potential gradient gives rise to the Joule/Ohmic heating in the solid electrode, q_{ohm} (J/m^3/s). We ignore the contributions of heat transfer due to mixing, which is associated with concentration gradients within the active material and CBD, and heat of phase change. Both are insignificant compared to the Ohmic heat, reaction heat and entropic heat.[2] Binder decomposition and side reactions between the active material and CBD are ignored as well.

An equivalent representation of this composite particle is a homogeneous sphere of radius r_2 that has density ρ^*, heat capacity c_p^*, diffusion coefficient D^*, ionic conductivity K^* and thermal conductivity λ^*. These characteristics are such that, for a given outer surface temperature, the two spheres have the same heat flux from the electrolyte across their outer surfaces and the same amount of heat release (while enforcing mass and charge conservation). Our goal is to express these equivalent parameters in terms of the volume fractions ($V_1 = r_1^3/r_2^3$ and $V_2 = 1 - V_1$) and physical and electrochemical properties of each phase.

Heat transfer in active core and CBD coating.—Given the composite particle's geometry, we deploy a spherical coordinate system $\mathbf{r} = (r, \theta, \phi)^T$. Spatiotemporal evolution of temperatures (K) in the active material, $T_1(\mathbf{r}, t)$ with $0 \leqslant r \leqslant r_1$, and the CBD coating, $T_2(\mathbf{r}, t)$ with $r_1 \leqslant r \leqslant r_2$, is described by heat equations,[1]

$$\rho_i c_{p_i} \frac{\partial T_i}{\partial t} = -\nabla \cdot \mathbf{J}_{heat,i} + q_{ohm,i},$$
$$\mathbf{J}_{heat,i} = -\lambda_i \nabla T_i, \qquad i = 1, 2. \tag{1}$$

Here, $q_{ohm,i}$ is the irreversible Ohmic heat generation induced by the ionic resistance under the gradients of electric potentials in each phase, $\phi_1(\mathbf{r}, t)$ with $0 \leqslant r \leqslant r_1$ and $\phi_2(\mathbf{r}, t)$ with $r_1 \leqslant r \leqslant r_2$,

$$q_{ohm,i} = K_i \nabla \phi_i \cdot \nabla \phi_i, \qquad i = 1, 2. \tag{2}$$

Equations 1 and 2 are defined on $0 < r < r_1$ for $i = 1$, and on $r_1 < r < r_2$ for $i = 2$; both for time $t > 0$. They are coupled by enforcing the continuity of the temperatures, T_i, and the energy balance at the interface $r = r_1$,

$$T_1(r_1, t) = T_2(r_1, t), \tag{3}$$

and

$$\lambda_1 \frac{\partial T_1}{\partial r}(r_1, t) - \lambda_2 \frac{\partial T_2}{\partial r}(r_1, t) = \mathcal{Q}_{int}(r_1, t),$$
$$\mathcal{Q}_{int} = \mathcal{Q}_{reac}(r_1, t) + \mathcal{Q}_{entr}(r_1, t). \tag{4}$$

The irreversible reactive heat flux at the interface $r = r_1$,

$$\mathcal{Q}_{reac} = J_1 \cdot [\phi_1 - \phi_2 - U(c_1/c_{1,max}, T)], \tag{5}$$

relates the intercalation current density $J_1(r_1, t)$ (A/m^2) to the activation overpotential $\phi_1(r_1, t) - \phi_2(r_1, t) - U(c_1(r_1, t)/c_{1,max})$. Here, U is the open circuit potential (V) that depends on both the Li filling fraction $c_1/c_{1,max}$ and temperature T; $c_1(r, t)$ is the Li concentration (mol/m^3); and $c_{1,max}$ is the maximum Li concentration that could be stored in the active particle. The reversible entropic heat flux,

$$\mathcal{Q}_{entr} = J_1 T_1 \frac{\partial U(c_1/c_{1,max}, T)}{\partial T}, \tag{6}$$

is induced by intercalation/de-intercalation of Li ions at the active particle surface $r = r_1$.

At the interface between the composite particle and liquid electrolyte, $r = r_2$, both temperature and the radial component of heat flux are continuous,

$$T_e(r_2, t) = T_2(r_2, t), \qquad \lambda_e \frac{\partial T_e}{\partial r}(r_2, t) = \lambda_2 \frac{\partial T_2}{\partial r}(r_2, t). \tag{7}$$

Here, $T_e(\mathbf{r})$ with $r \geqslant r_2$ is the electrolyte temperature, and λ_e denotes the thermal conductivity of the electrolyte. The problem formulation is completed by specifying the boundary and initial conditions

$$T_1(r = 0, t) < \infty\ ; \qquad T_i(\mathbf{r}, 0) = T_{in}, \quad i = 1, 2. \tag{8}$$

Heat transfer in equivalent particle.—The equivalent model treats the composite particle as a homogeneous material with equivalent density ρ^*, heat capacity c_p^*, and thermal conductivity λ^*, etc. (Fig. 1). Equations 1 and 2 are replaced with

$$\rho^* c_p^* \frac{\partial T}{\partial t} = -\nabla \cdot \mathbf{J}_{heat}^* + q_{ohm}^*, \quad \mathbf{J}_{heat}^* = -\lambda^* \nabla T \tag{9}$$

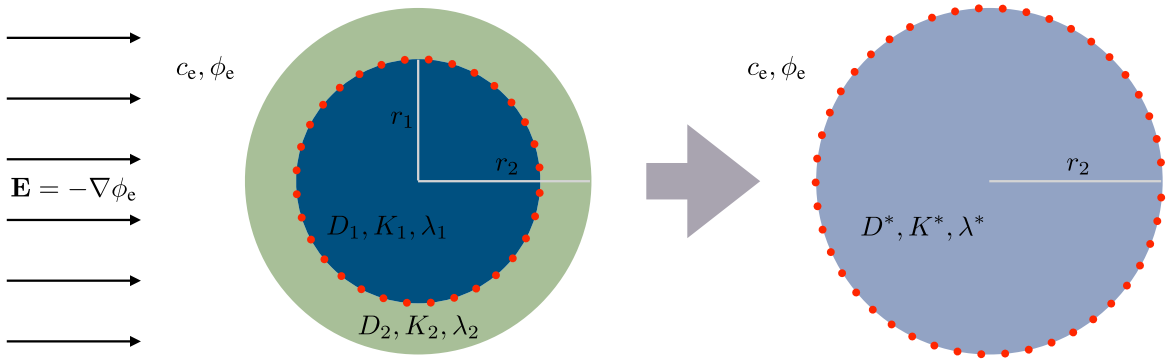

Figure 1. Left: Spherical composite particle of radius r_2 comprising an active material core of radius r_1 coated with a CBD layer. The active material has diffusion coefficient D_1, ionic conductivity K_1, and thermal conductivity λ_1; the corresponding quantities for CBD are denoted by D_2, K_2, and λ_2. Right: Its homogeneous counterpart with equivalent diffusion coefficient D^*, ionic conductivity K^*, and thermal conductivity λ^*. The red lines denote locations of the intercalation surface. The sphere is immersed in an electrolyte with Li-ion concentration c_e, electric potential ϕ_e, and uniform electric field $\mathbf{E} = -\nabla\phi_e$.

and

$$q^*_{\text{ohm}} = \mathcal{K}_h K^* \nabla\phi \cdot \nabla\phi. \quad [10]$$

These equations describe the spatiotemporal evolution of temperature, $T(\mathbf{r}, t)$, in the equivalent homogeneous particle, i.e., for $0 < r < r_2$. The Ohmic heat generation, q^*_{ohm}, involves the equivalent ionic conductivity K^* (S/m) and the ionic conductivity correction factor $\mathcal{K}_h$ (-). The latter is determined below by requiring the amount of heat flux entering the composite and homogenized particles at $r = r_2$ to be the same.

The interfacial and boundary conditions 3–7 are replaced with the boundary conditions at $r = r_2$,

$$T_e(r_2, t) = T(r_2, t), \quad [11a]$$

$$\lambda^* \frac{\partial T}{\partial r}(r_2, t) - \lambda_e \frac{\partial T_e}{\partial r}(r_2, t) = \mathcal{Q}^*_{\text{int}}(r_2, t),$$
$$\mathcal{Q}^*_{\text{int}} = \mathcal{Q}^*_{\text{reac}}(r_2, t) + \mathcal{Q}^*_{\text{entr}}(r_2, t). \quad [11b]$$

The equivalent reactive heat flux, $\mathcal{Q}^*_{\text{reac}}$, and entropic heat flux, $\mathcal{Q}^*_{\text{entr}}$, at the electrolyte-solid interface $r = r_2$ are given by

$$\mathcal{Q}^*_{\text{reac}} = J \cdot [\phi - \phi_e - U(c/c_{\max}, T)], \quad [12]$$

$$\mathcal{Q}^*_{\text{entr}} = JT \frac{\partial U(c/c_{\max}, T)}{\partial T}. \quad [13]$$

The intercalation current density, $J(r_2, t)$ (A/m^2), and the maximum Li concentration that can be stored in the homogenized particle, $c_{\max}$, are chosen to ensure their consistency with the composite particle.[25] Boundary and initial conditions 8 are replaced with

$$T(r = 0, t) < \infty \; ; \; \phi(r = 0, t) < \infty \; ; \; T(\mathbf{r}, 0) = T_{\text{in}}. \quad [14]$$

Thermal problems 1–8 and 9–14 are coupled with heat transfer equations for the electrolyte and with transport equations for both the solid particles and the electrolyte. The following simplifying assumptions facilitate the derivation of the effective properties of a composite particle. First, since interfacial conditions 7 and 11 hold for all values of the liquid electrolyte temperature at the interface, $T_e(r_2, \cdot)$, we treat the latter as given rather than computed from the heat transport equation in the liquid electrolyte.[25] Second, while some relevant transport parameters, such as diffusion coefficients and intercalation rates, are concentration- and temperature-dependent, we treat them as piece-wise constants. This is consistent with the state-of-the-art pseudo two-dimensional (P2D) models of electrochemical transport in batteries (e.g., Ref. 26 and references therein); rather than dealing with concentration-dependent diffusion coefficients, $D = D(c)$, these models use different constant values D for different values of the state of charge, $c(r_2, t)/c_{\max}$. Third, we consider a constant current density $\mathbf{i}$ with magnitude I (A/m^2) at the electrode/electrolye interface, $r = r_2$ (Fig. 1) and assume azimuthal symmetry.

Equivalent Thermal Properties of Solid Phase

The density and heat capacity of the equivalent homogeneous particle are computed as[27]

$$\rho^* = \rho_1 V_1 + \rho_2 V_2, \quad [15]$$

$$c^*_p = \frac{V_1 \rho_1 c_{p_1} + V_2 \rho_2 c_{p_2}}{\rho_1 V_1 + \rho_2 V_2}. \quad [16]$$

These and other relations are derived by ensuring that the homogenized particle retains key integral characteristics of the original composite particle. For example, the requirement that the two particles have the same total Li-ion intercalation flux yields (Eq. 17 in Ref. 25)

$$r_1^2 J_1(r_1, t) = r_2^2 J(r_2, t - \tau_D) \mathcal{H}(t - \tau_D), \quad [17]$$

where $\mathcal{H}(\cdot)$ is the Heaviside function, and the reaction delay time $\tau_D = (r_2 - r_1)^2/D_2$ accounts for the shift of the intercalation interface from the inner radius $r = r_1$ to the outer radius $r = r_2$. The thermal conductivity of an equivalent medium is known to exhibit transitory effects at early times.[28] We define $\lambda^*(t)$ and $\mathcal{K}_h(t)$ as the thermal conductivity and the ionic conductivity correction factor of the homogenized sphere that produce the average temperature $\bar{T}(t)$ corresponding to the average temperature of the composite sphere, i.e.,

$$\frac{4\pi r_2^3}{3} \bar{T}(t) = \int_0^{r_2} T(r, t)\, r^2 \, dr = \int_0^{r_1} T_1(r, t)\, r^2 \, dr + \int_{r_1}^{r_2} \bar{T}_2(r, t) r^2 \, dr, \quad [18]$$

and satisfy the integral form of the energy balance in 17. In the Appendix, we derive integral equations satisfied by $\lambda^*(t)$ and $\mathcal{K}_h(t)$; after the transitory effects dissipate, these properties reach their constant asymptotes given by the weighted harmonic means of K_1 and K_2, and λ_1 and λ_2:

$$\frac{\mathcal{K}_h}{K^*} = \frac{V_1^{-1/3}}{K_1} + \frac{3a(1 - V_1^{4/3}) + 4b(1 - V_1) + 6c(1 - V_1^{2/3})}{4K_2} \quad [19]$$

and

$$\lambda^* = \left\{ \frac{(1 - V_1^{1/3})^3}{4\lambda_2 K_2} [15a((V_1^{1/3} + 1)^3 - V_1^{2/3} - V_1^{1/3}) + b(4(V_1^{1/3} + 1)^2 - V_1^{1/3}) + \frac{15c}{2}(V_1^{1/3} + 1)] + \frac{V_1^{1/3}}{\lambda_1 K_1} \right\}^{-1} \frac{\mathcal{K}_h}{K^*}. \quad [20]$$

Here, the functions $a(V_1)$, $b(V_1)$ and $c(V_1)$ are defined in Eq. A·26b of the Appendix, and

$$K^* = \frac{2K_1 K_2}{K_1 \frac{V_1^{-1/3} - 1}{1 - V_1^{1/3}/(V_1^{1/3} + 1)^2} + 2K_2 / V_1^{1/3}} \quad [21]$$

is the equivalent ionic conductivity.[25] If the sphere consists entirely of the active material, i.e., if $V_1 = 1$, then these expressions reduce to $\mathcal{K}_h = 1$ and $\lambda^* = \lambda_1$, as they should.

Results and Discussion

The ionic conductivity correction factor $\mathcal{K}_h$ is introduced to ensure that the same amount of heat enters the composite and homogenized particles from the electrolyte, in the presence of the Ohmic heat generation in CBD, $q_{\text{ohm},2} = K_2 \nabla\phi_2 \cdot \nabla\phi_2$. Figure 2 exhibits the functional dependence, given by Eq. 19, of $\mathcal{K}_h$ on both the volume fraction of the active material in the mixture, V_1, and the physical properties of the active material and CBD. The latter properties are reported as the ratio of ionic conductivities, K_2/K_1, and the ratio of thermal conductivities, λ_2/λ_1. Since less Ohmic heat is generated in CBD than in the active material, the correction factor $\mathcal{K}_h$ decreases as V_1 increases (Fig. 2a), i.e., as the amount of CBD in the composite decreases. Since the equivalent ionic conductivity K^* increases with V_1 in accordance with Eq. 21, the ratio $\mathcal{K}_h/K^*$ decreases with V_1 (Fig. 2b).

The magnitude of the correction function $\mathcal{K}_h$ increases as the contrast between ionic conductivities of the CBD and active material, K_2/K_1, becomes more pronounced (Fig. 2a), due to the reduction in Ohmic heat generation in CBD. It follows from Eqs. 21

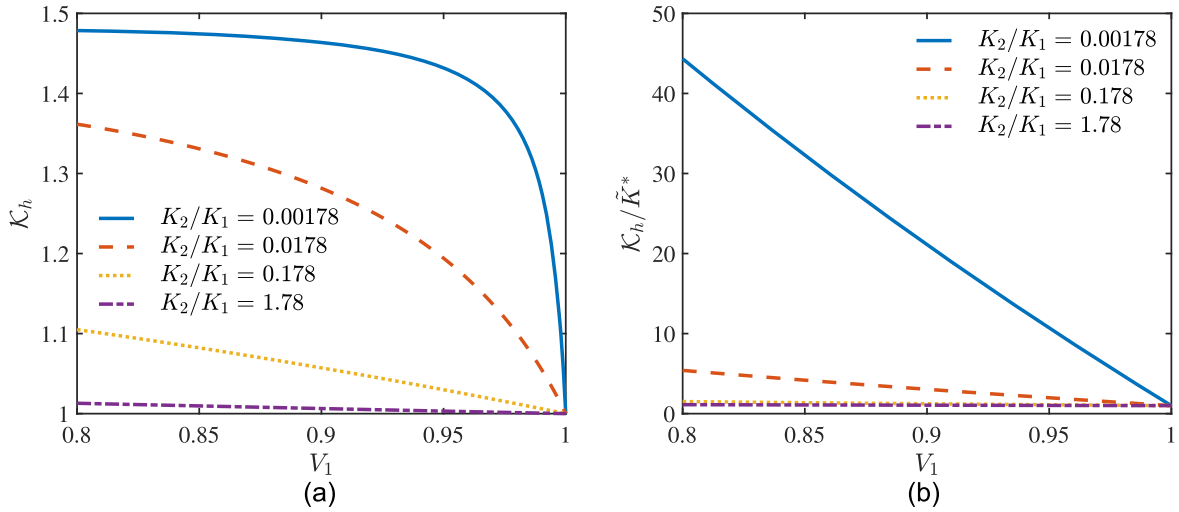

Figure 2. Dependence of (a) ionic conductivity corrector $\mathcal{K}_h$ and (b) its normalized counterpart $\mathcal{K}_h/\tilde{K}^*$ on the volume fraction of the active material in the composite, V_1. It is computed with Eq. 19 for the thermal conductivity ratio $\lambda_2/\lambda_1 = 0.01$ and the ionic conductivity ratios $K_2/K_1 = 0.00178$, 0.0178, 0.178 and 1.78. In (b), $\tilde{K}^* = K^*/K_1$ denotes the equivalent ionic conductivity of the homogeneous particle normalized with the ionic conductivity of the active material.

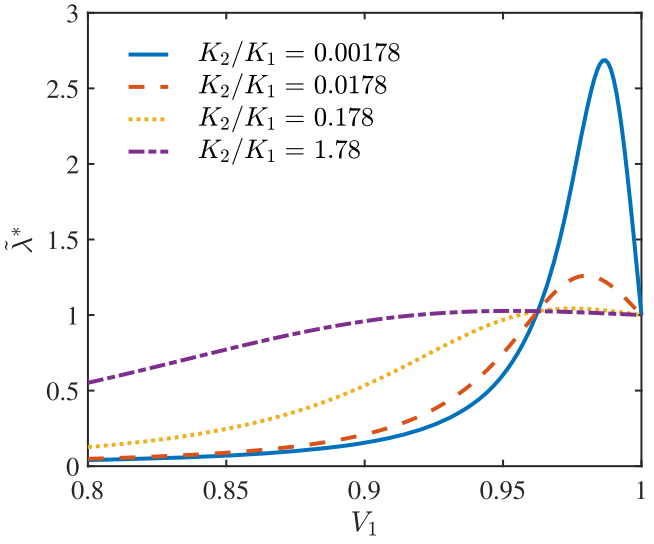

Figure 3. Dependence of equivalent thermal conductivity λ^*, normalized with the active material's thermal conductivity λ_1, on the volume fraction of the active material in the composite, V_1. It is computed with Eq. 20 for the thermal conductivity ratio $\lambda_2/\lambda_1 = 0.01$ and the ionic conductivity ratios $K_2/K_1 = 0.00178$, 0.0178, 0.178 and 1.78.

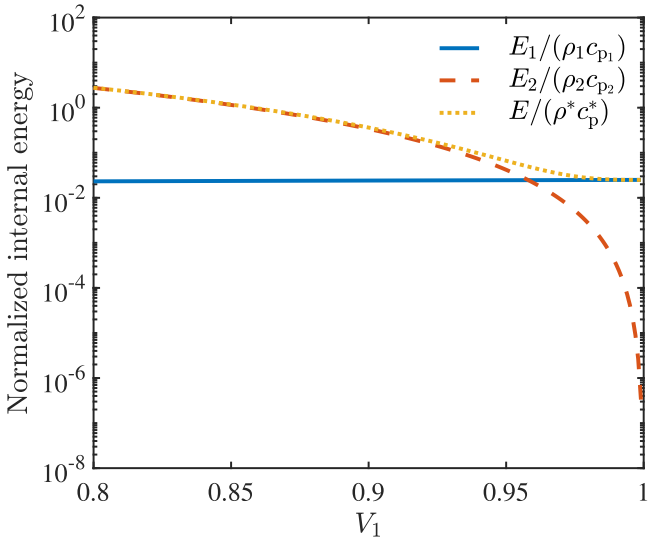

Figure 4. Internal energy, normalized by respective volumetric heat capacity, in the active material, $E_1/(\rho_1 c_{p_1})$, in CBD, $E_2/(\rho_2 c_{p_2})$, and in the homogeneous particle, $E/(\rho^* c_p^*)$, as function of the volume fraction of the active material in the composite, V_1. The ratios of the ionic conductivity and thermal conductivity are set to $K_2/K_1 = 0.0178$ and $\lambda_2/\lambda_1 = 0.01$, respectively.

and 19 that, for a fixed K_1,

$$\lim_{K_2 \to \infty} \mathcal{K}_h = 1 \qquad [22]$$

and

$$\lim_{K_2 \to \infty} \mathcal{K}_h / \tilde{K}^* = V_1^{-1/3}/K_1, \qquad [23]$$

as no Ohmic heat is generated in CBD with large ionic conductivity ($K_2 \to \infty$).

Figure 3 exhibits the dependence of equivalent thermal conductivity λ^*—normalized with the active material's thermal conductivity, λ_1—on the volume fraction of the active material in the composite, V_1. The function $\tilde{\lambda}^*(V_1) \equiv \lambda^*(V_1)/\lambda_1$ is computed with Eq. 20, for the thermal conductivity ratio $\lambda_2/\lambda_1 = 0.01$ and several values of the ionic conductivity ratio K_2/K_1. The function $\tilde{\lambda}^* = \tilde{\lambda}^*(V_1)$ is non-monotonic: $\tilde{\lambda}^*$ first increases and then decreases with V_1, reaching $\tilde{\lambda}^* = 1$ when $V_1 = 1$. The maximum value of $\tilde{\lambda}^* = \tilde{\lambda}^*(V_1)$ in Eq. 20 is attained at $V_1^{\max}$ for which $\partial\lambda^*/\partial V_1 = 0$. The maximum thermal conductivity of the mixture is $\lambda^*_{\max} = \lambda^*(V_1^{\max})$.

To gain physical insight into this non-monotonic behavior of $\tilde{\lambda}^*(V_1)$, we rewrite Eq. 18 as

$$E = \frac{\rho^* c_p^*}{\rho_1 c_{p_1}} E_1 + \frac{\rho^* c_p^*}{\rho_2 c_{p_2}} E_2, \qquad [24]$$

in terms of the internal energies (J/m^3) in the active material, CBD and the homogeneous particle,

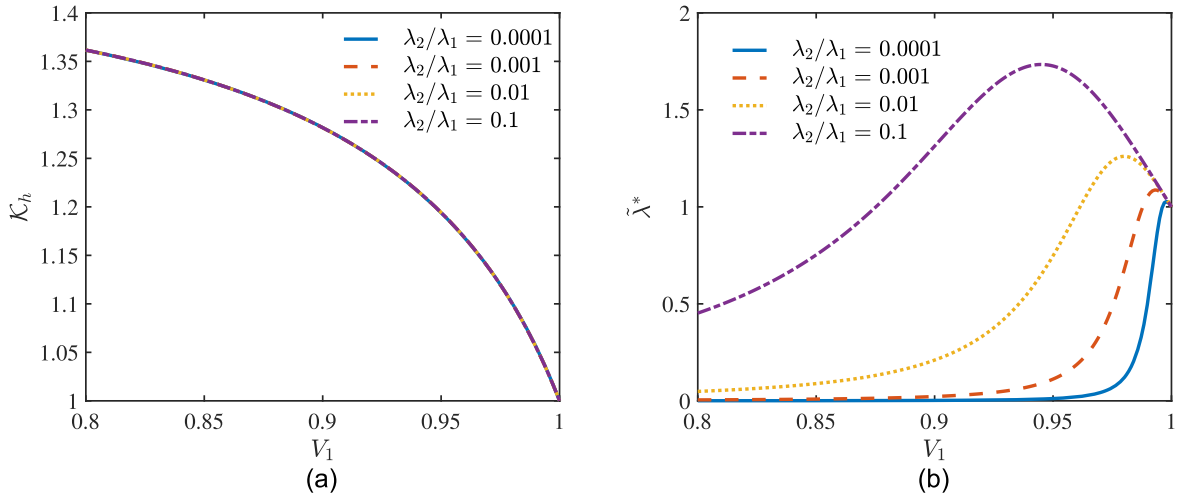

Figure 5. Dependence of **(a)** ionic conductivity corrector $\mathcal{K}_h$ and **(b)** normalized equivalent thermal conductivity $\tilde{\lambda}^*$ on the volume fraction of the active material in the composite, V_1. The graphs are computed with Eqs. 19 and 20, for the ionic conductivity ratio $K_2/K_1 = 0.0178$ and the thermal conductivity ratios $\lambda_2/\lambda_1 = 0.0001$, 0.001, 0.01 and 0.1.

$$E_1 = \rho_1 c_{p_1} \int_0^{r_1} T_1(r,\, t)\, r^2\, \mathrm{d}r,$$
$$E_2 = \rho_2 c_{p_2} \int_{r_1}^{r_2} \bar{T}_2(r,\, t)\, r^2\, \mathrm{d}r,$$
$$E = \rho^* c_p^* \int_0^{r_2} T(r,\, t)\, r^2\, \mathrm{d}r, \qquad [25]$$

respectively. The expressions for the temperature distribution in the active material, CBD, and the homogeneous particle are given by Eqs. A·35–A·36 in the Appendix. The dependence of these energies on V_1 is plotted in Fig. 4, for $K_2/K_1 = 0.0178$ and $\lambda_2/\lambda_1 = 0.01$. When the active material volume fraction V_1 is small, $E_2/(\rho_2 c_{p_2}) \gg E_1/(\rho_1 c_{p_1})$ and $E/(\rho^* c_p^*) \approx E_2/(\rho_2 c_{p_2})$. Figure 4 reveals that both $E_2/(\rho_2 c_{p_2})$ and $E/(\rho^* c_p^*)$ exhibit an almost exponential decay with V_1. Consequently, the mean temperature in the homogeneous particle, $\bar{T} = \frac{3}{4\pi r_2^3} E/(\rho^* c\mathrm{p}^*)$, also decreases nearly exponentially. Since $\mathcal{K}_h/K^*$ decreases linearly with V_1 (Fig. 2), $\tilde{\lambda}^*$ increases with V_1 according to $\bar{T} = \frac{I^2 \mathcal{K}_h r_2^5}{45 \lambda^* K^*}$. In contrast, when V_1 is large, $E_1/(\rho_1 c_{p_1}) \gg E_2/(\rho_2 c_{p_2})$ and $E/(\rho^* c_p^*) \approx E_1/(\rho_1 c_{p_1})$. As V_1 continues to increase, $E_1/(\rho_1 c_{p_1})$ and $E/(\rho^* c_p^*)$ experience a slight increase and, thus, the mean temperature in the homogeneous particle increases as well. Furthermore, since $\mathcal{K}_h/K^*$ decreases with V_1 (Fig. 2) for large values of V_1, $\tilde{\lambda}^*$ decreases with V_1.

For a given small V_1, smaller values of the ionic conductivity ratio K_2/K_1 give rise to smaller values of the effective thermal conductivity λ^* (Fig. 3). Large values of V_1 have the opposite effect: smaller values of K_2/K_1 induce larger values of λ^*. That is because $E/(\rho^* c_p^*) \approx E_2/(\rho_2 c_{p_2})$ when V_1 is small (Fig. 4). Combining Eqs. 19, 25, A·35b and A·36, we obtain

$$\lambda^* \propto \frac{K_2}{K_1} V_1^{-1/3} + \frac{3a}{4}(1 - V_1^{4/3}) + b(1 - V_1) + \frac{3c}{2}(1 - V_1^{2/3}), \qquad [26]$$

which shows that λ^* increases linearly with K_2/K_1. On the other hand, if V_1 is large, $E/(\rho^* c_p^*) \approx E_1/(\rho_1 c_{p_1})$ and the mean temperature of the homogeneous particle is independent of K_2. Since smaller values of K_2/K_1 correspond to larger values of $\mathcal{K}_h/K^*$ (Fig. 2), λ^* decreases with K_2/K_1 when V_1 is large.

Figure 3 also suggests the existence of a critical value of V_1, denoted by V_1^{cr} ($0 < V_1^{\mathrm{cr}} < 1$), for which λ^* becomes independent of K_2/K_1. This critical value V_1^{cr} is a solution of the algebraic equation

$$\frac{3\lambda_2 V_1^{2/3}}{\lambda_1 (1 - V_1^{1/3})^3}[a(1 - V_1^{4/3}) + 4b(1 - V_1)/3 + 2c(1 - V_1^{2/3})] = 15a[(V_1^{1/3} + 1)^3 - V_1^{2/3} - V_1^{1/3}] + b[4(V_1^{1/3} + 1)^2 - V_1^{1/3}] + \frac{15c}{2}(V_1^{1/3} + 1), \qquad [27]$$

which is derived from Eqs. 19 and 20. The critical volume fraction V_1^{cr} is a function of the thermal conductivity ratio λ_2/λ_1. When $V_1 = V_1^{\mathrm{cr}}$, the effective thermal conductivity $\tilde{\lambda}_{\mathrm{cr}}^* = V_1^{-2/3}$.

Figure 5 shows the dependence of ionic conductivity corrector $\mathcal{K}_h$ and equivalent thermal conductivity $\tilde{\lambda}^*$ on the volume fraction V_1 and the thermal conductivity ratio λ_2/λ_1. According to Eq. 19, $\mathcal{K}_h$ is independent of λ_2/λ_1, while the latter significantly affects $\tilde{\lambda}^*$, as predicted by Eq. 20.

Conclusions

We developed an equivalent heat-conduction model for the composite electrode consisting of a spherical active-material particle coated with CBD and immersed in a liquid electrolyte. The model replaces this composite sphere with a homogeneous sphere of equivalent thermal conductivity and with equivalent heat-generation terms (Joule/Ohmic heat, reactive heat, and entropic heat inside the particle and on its surface). The equivalent properties are defined such that, for a given outer surface temperature, the two spheres have the same heat across the solid/electrolyte interface and the same amount of heat release (while enforcing mass and charge conservation). Our key result is an analytical expression for the effective thermal conductivity, which is given in terms of the volume fraction of the active material in the composite and the electrochemical and thermal properties of the active material and CBD. Our analysis leads to the following major conclusions.

- Our model provides an easy-to-use means for quantitative assessment of CBD's impact on thermal properties of composite electrodes. Consider an electrode with CBD volume fraction of 0.1 and the ratios of thermal and ionic conductivities of CBD and active material of 0.01 and 0.0178, respectively. Ignoring CBD, as is current practice, would overestimate the composite's thermal conductivity by approximately 400%.

- The ionic conductivity factor in our model accounts for the Joule/Ohmic heat generation within CBD. It ensures that the same amount of heat enters both the composite and homogeneous particles. This factor equals 1 in the absence of Ohmic heat generation in CBD.
- Our expression for the effective thermal conductivity provides a valuable insight for the composite electrode's optimal design. It identifies the active material's volume fraction that maximizes the composite's thermal conductivity, for given thermal and ionic conductivity ratios between CBD and the active material.
- The simplicity of our equivalent electrochemical-thermal parameterization facilitates its integration into pore- and device-scale models of Li-ion and Li-metal batteries. These models can now account for the presence of CBD and the physicochemical characteristics of composite electrodes, without extra computational expense.

Physical insights gained from our study offer guidance for the optimal design of composite electrodes. Our effective model is not limited to studying the effects of CBD; it can also be extended to model novel composite anode and cathode materials, such as silicon coated with carbon or lithium iron phosphate coated with carbon. The use of our model to explore the thermal behavior of these materials will provide valuable information for their integration into advanced battery systems. In addition to composite electrodes, future work involves the study of thermal effects that impact dendrite growth and the formation of local hotspots in Li-metal and all-solid-state batteries.[29,30]

Acknowledgments

This work was supported in part by Air Force Office of Scientific Research under award number FA9550-21-1-0381, by Hyundai Motor Group, and by StorageX at Stanford University.

Appendix. Effective Thermal Conductivity

Making use of Eq. 17, we rewrite the heat flux $\mathcal{Q}_{\text{int}}(r_1, t)$ in 4 as

$$\mathcal{Q}_{\text{int}} = J(r_2, t-\tau_D)\frac{r_2^2}{r_1^2}\mathcal{H}(t-\tau_D) \times\left[\phi_1 - \phi_2 - U(\tilde{c}_1, T) + T_1\frac{\partial U(\tilde{c}_1, T)}{\partial T}\right]_{|r=r_1} \quad [\text{A}\cdot1]$$

where $\tilde{c}_1(r, t) = c_1(r, t)/c_{1,\max}$. The requirement that the total amount of heat generated by (de)intercalation in the composite and homogenized particles be the same translates into

$$r_1^2\int_0^\pi\int_0^{2\pi}\mathcal{Q}_{\text{int}}(r_1, t)\sin\theta\,\text{d}\varphi\text{d}\theta = r_2^2\int_0^\pi\int_0^{2\pi}\mathcal{Q}^*_{\text{int}}(r_2, t-\tau)\mathcal{H}(t-\tau_D)\sin\theta\,\text{d}\varphi\text{d}\theta. \quad [\text{A}\cdot2]$$

The derivation of the effective ionic conductivity K^* ensures that[25]

$$\phi_1(r_1, t) - \phi_2(r_1, t) = \phi(r_2, t) - \phi_e(r_2, t). \quad [\text{A}\cdot3]$$

By imposing the condition

$$T_1(r = r_1, t) = T(r = r_2, t-\tau_D), \quad [\text{A}\cdot4]$$

we ensure that the effective diffusion coefficient D^* satisfies the conditions[25]

$$U(\tilde{c}_1(r_1, t), T_1(r_1, t)) = U(\tilde{c}(r_2, t-\tau_D), T(r_2, t-\tau_D)), \quad [\text{A}\cdot5]$$

$$\frac{\partial U(\tilde{c}_1, T)}{\partial T}(r_1, t) = \frac{\partial U(\tilde{c}, T)}{\partial T}(r_2, t-\tau_D), \quad [\text{A}\cdot6]$$

where $\tilde{c}(r, t) = c(r, t)/c_{\max}$, by construction. These conditions on the intercalation surfaces of the composite ($r = r_1$) and homogenized ($r = r_2$) particles automatically satisfy Eq. A·2. This result enables us to define the effective thermal conductivity λ^*. Indeed, accounting for Eq. 11b and the interfacial relations A·3–A·6, we obtain an equation for $\lambda^*(t)$,

$$\frac{r_1^2}{r_2^2}\int_0^\pi\int_0^{2\pi}\left[\lambda_1\frac{\partial T_1}{\partial r} - \lambda_2\frac{\partial T_2}{\partial r}\right]_{(r_1,t)}\sin\theta\,\text{d}\varphi\text{d}\theta = \mathcal{H}(t-\tau_D)\int_0^\pi\int_0^{2\pi}\left[\lambda^*\frac{\partial T}{\partial r} - \lambda_2\frac{\partial T_2}{\partial r}\right]_{(r_2,t-\tau_D)}\sin\theta\,\text{d}\varphi\text{d}\theta. \quad [\text{A}\cdot7]$$

It remains to compute the temperature gradients in the homogenized and composite particles.

In the derivations below, we take the outer surface temperature $T_e(r_2, t)$ to be constant $T_e = T_{\text{in}}$. Without loss of generality, we set the initial temperature to $T_{\text{in}} = 0$ (otherwise, one can repeat our analysis for $T_i - T_{\text{in}}$ and $T - T_{\text{in}}$). The continuity conditions at the interfaces $r = r_1$ and $r = r_2$ become

$$T_1(r = r_1, t) = \bar{T}_2(r = r_1, t) = \bar{T}_2(r = r_2, t) = 0, \quad [\text{A}\cdot8]$$

where $\bar{T}_2(r, t) = (1/2)\int_0^\pi T_2(r, \theta, t)\sin\theta\,\text{d}\theta$ is the angle-average temperature.

A.1. Temperature in equivalent sphere.—Given the azimuthal and polar symmetry, Eq. 9 takes the form

$$\rho^* c_p^*\frac{\partial T}{\partial t} = \frac{\lambda^*}{r^2}\frac{\partial}{\partial r}\left(r^2\frac{\partial T}{\partial r}\right) + q^*_{\text{ohm}}. \quad [\text{A}\cdot9]$$

The assumption of azimuthal and polar symmetry enables one to solve the Laplace equations for electric potentials in polar coordinates,[25] transforming Eq. 10 into $q^*_{\text{ohm}} = \mathcal{K}_h K^*\nabla\phi\cdot\nabla\phi = \mathcal{K}_h(K^*\nabla\phi\cdot K^*\nabla\phi)/K^* = \mathcal{K}_h(-\mathbf{i})\cdot(-\mathbf{i})/K^* = I^2\mathcal{K}_h/K^*$. This equation is rewritten in terms of the rescaled time,

$$\mathcal{T} = \int_0^t \lambda^*(t')\,\text{d}t', \quad [\text{A}\cdot10]$$

and the new dependent variable $u(r, t) = rT(r, t)$ as

$$\frac{\partial u}{\partial\mathcal{T}} = \frac{1}{\rho^* c_p^*}\frac{\partial^2 u}{\partial r^2} + \frac{I^2 r\mathcal{K}_h}{\lambda^*(h(\mathcal{T}))\rho^* c_p^* K^*}, \qquad 0 < r < r_2, \quad [\text{A}\cdot11]$$

where $\mathcal{K}_h = \mathcal{K}_h(h(\mathcal{T}))$ and $\lambda^* = \lambda^*(h(\mathcal{T}))$, and $t = h(\mathcal{T})$ is given implicitly by Eq. A·10. Accounting for the boundary and initial conditions 14 with $T_{\text{in}} = 0$, the Laplace-transformed (with respect to $\mathcal{T}$) solution of Eq. A·11 is

$$\hat{u}(r, \lambda_{\mathcal{T}}) = A(\text{e}^{r\sqrt{s}} - \text{e}^{-r\sqrt{s}}) + \frac{I^2 r}{\rho^* c_p^* K^*}\int_0^\infty\frac{\mathcal{K}_h}{\lambda^*}\text{e}^{-\lambda_{\mathcal{T}}\mathcal{T}}\text{d}\mathcal{T}, \quad [\text{A}\cdot12]$$

where $\lambda_{\mathcal{T}}$ is the Laplace-transform variable, and $s = \lambda_{\mathcal{T}}\rho^* c_p^*$. The constant of integration A is obtained from the Laplace transform of the boundary condition 11a, $\hat{u}(r_2, \lambda_{\mathcal{T}}) = 0$:

$$A = -\frac{1}{\text{e}^{r_2\sqrt{s}} - \text{e}^{-r_2\sqrt{s}}}\frac{I^2 r_2}{\rho^* c_p^* K^*}\int_0^\infty\frac{\mathcal{K}_h}{\lambda^*}\text{e}^{-\lambda_{\mathcal{T}}\mathcal{T}}\,\text{d}\mathcal{T}. \quad [\text{A}\cdot13]$$

This yields the Laplace-transformed temperature in the equivalent sphere

$$\hat{T}(r,\lambda_{\mathcal{T}}) = \frac{I^2}{\rho^* c_{\mathrm{p}}^* K^*}\left[1 - \frac{\mathrm{e}^{r\sqrt{s}} - \mathrm{e}^{-r\sqrt{s}}}{\mathrm{e}^{r_2\sqrt{s}} - \mathrm{e}^{-r_2\sqrt{s}}}\frac{r_2}{r}\right] \times \int_0^\infty \frac{\mathcal{K}_h}{\lambda^*}\mathrm{e}^{-\lambda_{\mathcal{T}}\mathcal{T}}\,\mathrm{d}\mathcal{T}. \quad [A\cdot14]$$

The inverse Laplace transform, $\mathcal{L}_{\mathcal{T}}^{-1}$, of $\hat{T}(r,\lambda_{\mathcal{T}})$ is given by the convolution,

$$T(r,\mathcal{T}) = \frac{I^2}{\rho^* c_{\mathrm{p}}^* K^*}\int_0^{\mathcal{T}} \frac{\mathcal{K}_h(h(\nu))}{\lambda^*(h(\nu))} w(r,\mathcal{T}-\nu)\mathrm{d}\nu, \quad [A\cdot15a]$$

where

$$w(r,\mathcal{T}) = \mathcal{L}_{\mathcal{T}}^{-1}\left\{1 - \frac{r_2\sinh(r\sqrt{s})}{r\sinh(r_2\sqrt{s})}\right\}. \quad [A\cdot15b]$$

A.2. Temperature in Composite Sphere.—*A.2.1. Solution for active material.*—Given the azimuth and polar symmetry, Eq. 1 with $i = 1$ takes the form

$$\rho_1 c_{\mathrm{p}_1}\frac{\partial T_1}{\partial t} = \frac{\lambda_1}{r^2}\frac{\partial}{\partial r}\left(r^2\frac{\partial T_1}{\partial r}\right) + q_{\mathrm{ohm},1}, \quad [A\cdot16]$$

where $q_{\mathrm{ohm},1} = (Ir_2^2/r_1^2)^2/K_1$. The transformation $u_1(r,t) = rT_1(r,t)$ turns Eq. A·16 into

$$\frac{\partial u_1}{\partial t} = \frac{\lambda_1}{\rho_1 c_{\mathrm{p}_1}}\frac{\partial^2 u_1}{\partial r^2} + \frac{q_{\mathrm{ohm},1}}{\rho_1 c_{\mathrm{p}_1}}r. \quad [A\cdot17]$$

Accounting for the initial and boundary conditions 8 with $T_{\mathrm{in}} = 0$, the Laplace-transformed solution of Eq. A·17 is

$$\hat{u}_1(r,\lambda) = A_1(\mathrm{e}^{\sqrt{s_1}\,r} - \mathrm{e}^{-\sqrt{s_1}\,r}) + \frac{q_{\mathrm{ohm},1}}{\lambda^2\rho_1 c_{\mathrm{p}_1}}r, \quad 0 \leqslant r \leqslant r_1, \quad [A\cdot18]$$

where λ is the Laplace variable, and $s_1 = \lambda\rho_1 c_{\mathrm{p}_1}/\lambda_1$. The constant of integration A_1 is obtained from the Laplace transforms of the auxiliary conditions 3and A·8:

$$A_1 = -\frac{q_{\mathrm{ohm},1}r_1}{\lambda^2\rho_1 c_{\mathrm{p}_1}(\mathrm{e}^{\sqrt{s_1}\,r_1} - \mathrm{e}^{-\sqrt{s_1}\,r_1})}. \quad [A\cdot19]$$

The Laplace-transformed temperature in the active material is

$$\hat{T}_1(r,\lambda) = -\frac{I^2 r_2^4/r_1^4}{\lambda^2\rho_1 c_{\mathrm{p}_1} r K_1}[\alpha_1(\mathrm{e}^{r\sqrt{s_1}} - \mathrm{e}^{-r\sqrt{s_1}}) - r], \quad 0 \leqslant r \leqslant r_1. \quad [A\cdot20]$$

A.2.2. Solution for CBD.—Unlike the Ohmic heat generation in the active material, $q_{\mathrm{ohm},1}$, the Ohmic heat generation in CBD, $q_{\mathrm{ohm},2} = K_2\nabla\phi_2\cdot\nabla\phi_2$, is a function of both distance r and polar angle θ. It is computed from the solutions of the Laplace equation for electric potential in polar coordinates,[25]

$$q_{\mathrm{ohm},2} = K_2[(a_2 - 2b_2 r^{-3})^2\cos^2\theta + (a_2 + b_2 r^{-3})^2\sin^2\theta], \quad [A\cdot21a]$$

with

$$a_2 = \frac{I(1 - r_1/r_2)}{K_2(1 - r_1^3/r_2^3)} = \frac{I(1 - V_1^{1/3})}{K_2(1 - V_1)}, \quad [A\cdot21b]$$

$$b_2 = \frac{I(r_1^3 - r_1 r_2^2)}{2K_2(1 - r_1^3/r_2^3)} = \frac{I(V_1 - V_1^{1/3})r_2^3}{2K_2(1 - V_1)}. \quad [A\cdot21c]$$

The angle-averaged Ohmic heat generation in CBD, $\bar{q}_{\mathrm{ohm},2}(r)$, is

$$\bar{q}_{\mathrm{ohm},2} = \frac{1}{2}\int_0^\pi q_{\mathrm{ohm},2}(r,\theta)\sin\theta\,\mathrm{d}\theta = K_2\left(a_2^2 + \frac{2b_2^2}{r^6}\right). \quad [A\cdot22]$$

Given the lack of polar symmetry, Eq. 1 with $i = 2$ is written as

$$\rho_2 c_{\mathrm{p}_2}\frac{\partial T_2}{\partial t} = \frac{\lambda_2}{r^2}\frac{\partial}{\partial r}\left(r^2\frac{\partial T_2}{\partial r}\right) + \frac{\lambda_2}{r^2\sin\theta}\frac{\partial}{\partial\theta}\left(\sin\theta\frac{\partial T_2}{\partial\theta}\right) + q_{\mathrm{ohm},2}. \quad [A\cdot23]$$

For the angle-averaged temperature, $\bar{T}_2(r,t)$, this gives

$$\rho_2 c_{\mathrm{p}_2}\frac{\partial\bar{T}_2}{\partial t} = \frac{\lambda_2}{r^2}\frac{\partial}{\partial r}\left(r^2\frac{\partial\bar{T}_2}{\partial r}\right) + \bar{q}_{\mathrm{ohm},2}. \quad [A\cdot24]$$

The transformation $\bar{u}_2(r,t) = r\bar{T}_2(r,t)$ turns Eq. A·24 into

$$\frac{\partial\bar{u}_2}{\partial t} = \frac{\lambda_2}{\rho_2 c_{\mathrm{p}_2}}\frac{\partial^2\bar{u}_2}{\partial r^2} + \frac{\bar{q}_{\mathrm{ohm},2}}{\rho_2 c_{\mathrm{p}_2}}r, \quad r_1 < r < r_2. \quad [A\cdot25]$$

As the CBD thickness, $r_2 - r_1$, is much smaller than the composite particle radius r_2, we approximate the inhomogeneous term in Eq. A·25 via a Taylor series expansion around $r = r_2$,

$$\frac{\bar{q}_{\mathrm{ohm},2}}{\rho_2 c_{\mathrm{p}_2}}r \approx \frac{K_2}{\rho_2 c_{\mathrm{p}_2}}\left\{a_2^2 r + 2b_2^2\left[\frac{1}{r_2^5} - \frac{5}{r_2^6}(r - r_2) + \frac{15}{r_2^7}(r - r_2)^2 + \mathcal{O}[(r - r_2)^3]\right]\right\} = \frac{I^2}{\rho_2 c_{\mathrm{p}_2}K_2}\left(\frac{ar^2}{r_2} + br + cr_2 + \mathcal{O}[(r - r_2)^3]\right), \quad [A\cdot26a]$$

with

$$a = \frac{15(V_1 - V_1^{1/3})^2}{2(1 - V_1)^2}, \quad b = \frac{(1 - V_1^{1/3})^2}{(1 - V_1)^2} - \frac{35(V_1 - V_1^{1/3})^2}{2(1 - V_1)^2}, \quad c = \frac{21(V_1 - V_1^{1/3})^2}{2(1 - V_1)^2}. \quad [A\cdot26b]$$

Figure 6 demonstrates the accuracy of this approximation when the CBD thickness is small.

Accounting for the initial and boundary conditions 8 with $T_{\mathrm{in}} = 0$, the Laplace-transformed solution of Eq. A·25 is

$$\hat{\bar{u}}_2(r,\lambda) = A_2\,\mathrm{e}^{\sqrt{s_2}\,r} + B_2\,\mathrm{e}^{-\sqrt{s_2}\,r} + \hat{F}(r), \quad r_1 \leqslant r \leqslant r_2, \quad [A\cdot27]$$

where λ is the Laplace variable, $s_2 = \lambda\rho_2 c_{\mathrm{p}_2}/\lambda_2$, and

$$\hat{F}(r) = \frac{I^2}{\lambda^2\rho_2 c_{\mathrm{p}_2}K_2}\left(\frac{ar^2}{r_2} + br + cr_2 + \frac{2a}{s_2 r_2}\right). \quad [A\cdot28]$$

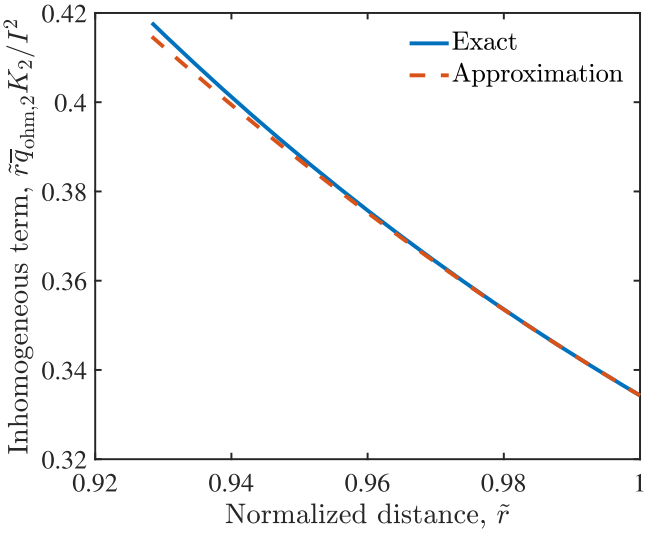

Figure 6. The non-dimensionalised inhomogeneous term $r\bar{q}_{\mathrm{ohm},2}(r)/(\rho_2 c_{\mathrm{p}_2})$ in Eq. A·25 and its approximation in Eq. A·26. Both are plotted against the normalized distance $\tilde{r} = r/r_2$.

The constants of integration A_2 and B_2 are obtained from the Laplace transforms of the auxiliary condition A·8, $\hat{\bar{u}}_2(r_1, \lambda) = \hat{\bar{u}}_2(r_2, \lambda) = 0$, as

$$A_2 = \frac{\hat{F}(r_2)\mathrm{e}^{-\sqrt{s_2}\,r_1} - \hat{F}(r_1)\mathrm{e}^{-\sqrt{s_2}\,r_2}}{\mathrm{e}^{-\sqrt{s_2}\,(r_2-r_1)} - \mathrm{e}^{\sqrt{s_2}\,(r_2-r_1)}}, \tag{A·29}$$

$$B_2 = \frac{\hat{F}(r_1)\mathrm{e}^{\sqrt{s_2}\,r_2} - \hat{F}(r_2)\mathrm{e}^{\sqrt{s_2}\,r_1}}{\mathrm{e}^{-\sqrt{s_2}\,(r_2-r_1)} - \mathrm{e}^{\sqrt{s_2}\,(r_2-r_1)}}. \tag{A·30}$$

Hence, the Laplace-transformed temperature in CBD is

$$\hat{\bar{T}}_2 = \frac{I^2}{\lambda^2\rho_2 c_{\mathrm{p}_2} r K_2}\Big[\alpha_2\mathrm{e}^{-(r_2-r)\sqrt{s_2}} + \beta_2\mathrm{e}^{-(r-r_1)\sqrt{s_2}} + \frac{ar^2}{r_2} + br + cr_2 + \gamma\Big], \quad r_1 \leqslant r \leqslant r_2, \tag{A·31a}$$

where $\gamma = 2a/(s_2 r_2)$,

$$\alpha_1 = \frac{r_1}{\mathrm{e}^{\sqrt{s_1}\,r_1} - \mathrm{e}^{-\sqrt{s_1}\,r_1}}, \tag{A·31b}$$

$$\alpha_2 = \frac{-(ar_1^2/r_2 + br_1 + cr_2 + \gamma) + (ar_2 + br_2 + cr_2 + \gamma)\mathrm{e}^{(r_2-r_1)\sqrt{s_2}}}{\mathrm{e}^{-\sqrt{s_2}\,(r_2-r_1)} - \mathrm{e}^{\sqrt{s_2}\,(r_2-r_1)}}, \tag{A·31c}$$

$$\beta_2 = \frac{-(ar_2 + br_2 + cr_2 + \gamma) + (ar_1^2/r_2 + br_1 + cr_2 + \gamma)\mathrm{e}^{(r_2-r_1)\sqrt{s_2}}}{\mathrm{e}^{-\sqrt{s_2}\,(r_2-r_1)} - \mathrm{e}^{\sqrt{s_2}\,(r_2-r_1)}}. \tag{A·31d}$$

and a, b and c are defined in Eq. A·26b.

A.3. Equations for equivalent thermal properties.— Substitution of Eq. A·15 into the definition of effecting properties λ^* and $\mathcal{K}_h$ in Eq. 18 yields two coupled nonlinear integral equations for $\lambda^*(t)$ and $\mathcal{K}_h = \mathcal{K}_h(t)$,

$$\frac{I^2}{\rho^* c_{\mathrm{p}}^* K^*}\int_0^{r_2}\int_0^{\mathcal{T}} \frac{\mathcal{K}_h(h(\nu))}{\lambda^*(h(\nu))} w(r, \mathcal{T}-\nu)\mathrm{d}\nu\; r^2\,\mathrm{d}r = \int_0^{r_1} T_1(r, t) r^2\,\mathrm{d}r + \int_{r_1}^{r_2} \bar{T}_2(r, t) r^2\,\mathrm{d}r, \tag{A·32}$$

$$\frac{r_1^2}{r_2^2}\left[\lambda_1\frac{\partial T_1}{\partial r} - \lambda_2\frac{\partial \bar{T}_2}{\partial r}\right]_{(r_1,t)} = \mathcal{H}(t-\tau_D)\left[\lambda^*\frac{\partial T}{\partial r} - \lambda_2\frac{\partial \bar{T}_2}{\partial r}\right]_{(r_2,t-\tau_D)}. \tag{A·33}$$

We compute the inverse Laplace transforms, $T_1(r_1, t)$ and $T_2(r_2, t)$, either numerically via the subroutine `INVLAP`[31] from the MATLAB File Exchange or analytically for large times t and steady state, as described below.

A.4. Asymptotic expressions for large time.— For large t, i.e., for small λ, the temperature in the composite sphere, Eq. A·31, behaves asymptotically as

$$\hat{T}_1(r, \lambda) = -\frac{I^2 r_2^4/r_1^4}{6\lambda_1\lambda K_1}[(r^2 - r_1^2) + \mathcal{O}(\lambda)], \tag{A·34a}$$

and

$$\hat{\bar{T}}_2(r, \lambda) = \frac{I^2}{12\lambda_2\lambda K_2} \times\Big\{ \frac{a}{r_2}[r_1^3 + r_1^2 r_2 + r_1 r_2^2 + r_2^3 - r^3 - (r_1^3 r_2 + r_1^2 r_2^2 + r_1 r_2^3)/r] + 2b[r_1^2 + r_2^2 + r_1 r_2 - r^2 - (r_1^2 r_2 + r_1 r_2^2)/r] + 6cr_2[r_1 + r_2 - r - r_1 r_2/r] + \mathcal{O}(\lambda^{1/2})\Big\}. \tag{A·34b}$$

The inverse Laplace transform is

$$T_1(r) = \frac{I^2 r_2^4/r_1^4}{6\lambda_1 K_1}(r_1^2 - r^2), \tag{A·35a}$$

and

$$\bar{T}_2(r) = \frac{I^2}{12\lambda_2 K_2} \times\Big\{\frac{a}{r_2}[r_1^3 + r_1^2 r_2 + r_1 r_2^2 + r_2^3 - r^3 - (r_1^3 r_2 + r_1^2 r_2^2 + r_1 r_2^3)/r] + 2b[r_1^2 + r_2^2 + r_1 r_2 - r^2 - (r_1^2 r_2 + r_1 r_2^2)/r] + 6cr_2[r_1 + r_2 - r - r_1 r_2/r]\Big\}. \tag{A·35b}$$

Similarly, the large-time asymptote of the temperature in the homogenized sphere is obtained from Eq. A·15 as

$$T(r) = \frac{I^2\mathcal{K}_h}{6\lambda^* K^*}(r_2^2 - r^2). \tag{A·36}$$

Substitution of Eqs. A·35 and A·36 into Eqs. A·32 and A·33 leads to

$$\frac{\mathcal{K}_h}{K^*} = \frac{1}{K_1\delta^2} + \frac{3a(1-\delta^4) + 4b(1-\delta^3) + 6c(1-\delta^2)}{4K_2} \tag{A·37}$$

and

$$\lambda^* = \left\{ \frac{(1-\delta)^3}{4\lambda_2 K_2} [15a((\delta \quad + 1)^3 - \delta^2 - \delta) + b(4(\delta+1)^2 - \delta) + \frac{15c}{2}(\delta+1) \right] + \frac{\delta}{\lambda_1 K_1} \Bigg\}^{-1} \frac{\mathcal{K}_h}{K^*}, \qquad [A\cdot38]$$

where $\delta = r_1/r_2$. Expressing these relations in terms of the volume fraction V_1 gives Eqs. 19 and 20.

ORCID

Weiyu Li https://orcid.org/0000-0002-7857-8115
Daniel M. Tartakovsky https://orcid.org/0000-0001-9019-8935

References

1. R. Kantharaj and A. M. Marconnet, "Heat generation and thermal transport in lithium-ion batteries: a scale-bridging perspective." *Nanoscale Microscale Thermophys. Eng.*, **23**, 128 (2019).
2. W. Gu and C. Wang, "Thermal-electrochemical modeling of battery systems." *J. Electrochem. Soc.*, **147**, 2910 (2000).
3. S. Zheng, L. Wang, X. Feng, and X. He, "Probing the heat sources during thermal runaway process by thermal analysis of different battery chemistries." *J. Power Sources*, **378**, 527 (2018).
4. M.-K. Tran, A. Mevawalla, A. Aziz, S. Panchal, Y. Xie, and M. Fowler, "A review of lithium-ion battery thermal runaway modeling and diagnosis approaches." *Processes*, **10**, 1192 (2022).
5. B. Yan, C. Lim, L. Yin, and L. Zhu, "Simulation of heat generation in a reconstructed LiCoO2 cathode during galvanostatic discharge." *Electrochim. Acta*, **100**, 171 (2013).
6. S. Al Hallaj and J. Selman, "A novel thermal management system for electric vehicle batteries using phase-change material." *J. Electrochem. Soc.*, **147**, 3231 (2000).
7. M. Song, Y. Hu, S.-Y. Choe, and T. R. Garrick, "Analysis of the heat generation rate of lithium-ion battery using an electrochemical thermal model." *J. Electrochem. Soc.*, **167**, 120503 (2020).
8. D. P. Finegan et al., "Characterising thermal runaway within lithium-ion cells by inducing and monitoring internal short circuits." *Energy Environ. Sci.*, **10**, 1377 (2017).
9. F. Larsson and B.-E. Mellander, "Abuse by external heating, overcharge and short circuiting of commercial lithium-ion battery cells." *J. Electrochem. Soc.*, **161**, A1611 (2014).
10. D. Abraham, E. Roth, R. Kostecki, K. McCarthy, S. MacLaren, and D. Doughty, "Diagnostic examination of thermally abused high-power lithium-ion cells." *J. Power Sources*, **161**, 648 (2006).
11. S. Wilke, B. Schweitzer, S. Khateeb, and S. Al-Hallaj, "Preventing thermal runaway propagation in lithium ion battery packs using a phase change composite material: an experimental study." *J. Power Sources*, **340**, 51 (2017).
12. D. Ouyang, J. Liu, M. Chen, J. Weng, and J. Wang, "An experimental study on the thermal failure propagation in lithium-ion battery pack." *J. Electrochem. Soc.*, **165**, A2184 (2018).
13. X. Yu, Z. Feng, Y. Ren, D. Henn, Z. Wu, K. An, B. Wu, C. Fau, C. Li, and S. J. Harris, "Simultaneous operando measurements of the local temperature, state of charge, and strain inside a commercial lithium-ion battery pouch cell." *J. Electrochem. Soc.*, **165**, A1578 (2018).
14. T. Heenan et al., "Mapping internal temperatures during high-rate battery applications." *Nature*, **617**, 507 (2023).
15. K. Shah, V. Vishwakarma, and A. Jain, "Measurement of multiscale thermal transport phenomena in Li-ion cells: a review." *J. Electrochem. Energy Convers. Storage*, **13**, 030801 (2016).
16. D. Bernardi, E. Pawlikowski, and J. Newman, "A general energy balance for battery systems." *J. Electrochem. Soc.*, **132**, 5 (1985).
17. C.-Y. Wang and V. Srinivasan, "Computational battery dynamics (CBD)-electro-chemical/thermal coupled modeling and multi-scale modeling." *J. Power Sources*, **110**, 364 (2002).
18. C.-F. Chen, A. Verma, and P. P. Mukherjee, "Probing the role of electrode microstructure in the lithium-ion battery thermal behavior." *J. Electrochem. Soc.*, **164**, E3146 (2017).
19. T. Katrašnik, I. Mele, and K. Zelič, "Multi-scale modelling of Lithium-ion batteries: From transport phenomena to the outbreak of thermal runaway." *Energy Convers. Manage.*, **236**, 114036 (2021).
20. A. Samba, N. Omar, H. Gualous, O. Capron, P. Van den Bossche, and J. Van Mierlo, "Impact of tab location on large format lithium-ion pouch cell based on fully coupled tree-dimensional electrochemical-thermal modeling." *Electrochim. Acta*, **147**, 319 (2014).
21. L. Liu, J. Park, X. Lin, A. M. Sastry, and W. Lu, "A thermal-electrochemical model that gives spatial-dependent growth of solid electrolyte interphase in a Li-ion battery." *J. Power Sources*, **268**, 482 (2014).
22. A. Vadakkepatt, B. L. Trembacki, S. R. Mathur, and J. Y. Murthy, "Effective thermal conductivity of lithium ion battery electrodes employing fully resolved simulations for use in volume averaged models." *Heat Transf. Summer Conf.*, **3**, HT2013 (2013).
23. A. Vadakkepatt, B. Trembacki, S. R. Mathur, and J. Y. Murthy, "Bruggeman's exponents for effective thermal conductivity of lithium-ion battery electrodes." *J. Electrochem. Soc.*, **163**, A119 (2015).
24. D. Oehler, P. Seegert, and T. Wetzel, "Modeling the thermal conductivity of porous electrodes of Li-ion batteries as a function of microstructure parameters." *Energy Technol.*, **9**, 2000574 (2021).
25. W. Li and D. M. Tartakovsky, "Effective representation of active material and carbon binder in porous electrodes." *J. Electrochem. Soc.*, **169**, 040556 (2022).
26. F. Boso, W. Li, K. Um, and D. M. Tartakovsky, "Impact of carbon binder domain on the performance of lithium-metal batteries." *J. Electrochem. Soc.*, **169**, 100550 (2022).
27. G. W. Milton, *The Theory of Composites; Cambridge Monographs on Applied and Computational Mathematics* (Cambridge University Press, Salt Lake City, Utah) (2002).
28. D. M. Tartakovsky and S. P. Neuman, "Transient effective hydraulic conductivities under slowly and rapidly varying mean gradients in bounded three-dimensional random media." *Water Resour. Res.*, **34**, 21 (1998).
29. W. Li, H. A. Tchelepi, Y. Ju, and D. M. Tartakovsky, "Stability-guided strategies to mitigate dendritic growth in lithium-metal batteries." *J. Electrochem. Soc.*, **169**, 060536 (2022).
30. W. Li, H. A. Tchelepi, and D. M. Tartakovsky, "Screening of electrolyte-anode buffers to suppress lithium dendrite growth in all-solid-state batteries." *J. Electrochem. Soc.*, **170**, 050510 (2023).
31. V. Juraj, "Numerical Inversion of Laplace Transforms in Matlab." MATLAB Central File (2023) https://www.mathworks.com/matlabcentral/fileexchange/32824-numerical-inversion-of-laplace-transforms-in-matlab.